A numerical method for conjugate heat transfer problems in hypersonic flows

(Article begins on next page)

28 April 2024

A Numerical Method For Conjugate Heat Transfer Problems in Hypersonic Flows

Pietro Ferrero[*] and Domenic D'Ambrosio[†]

Politecnico di Torino - DIASP, 10129 Torino, Italy

A finite-volume two-dimensional plane/axisymmetric heat-conduction solver for solid materials has been developed and coupled with a hypersonic flow solver to the aim of evaluating the thermal load on a body that is immersed in a high-speed flow. Different coupling strategies that can be enforced between the two solvers were considered and are discussed here. A tight coupling technique is particularly suitable for unsteady time-accurate calculations, but due to the large difference between fluid dynamics and heat conduction time scales, this may lead to unacceptable computational times. A valid alternative approach is to proceed with a series of "quasi-stationary" states, allowing the heat-conduction solver to evolve in a loosely coupled fashion using time steps which are large with respect to the flow time scale. The obtained results are compared with available numerical and experimental data, showing a fairy good agreement.

I. Introduction

The goal of heat transfer studies is the accurate prediction of temperature and heat flux distribution in space and time in a body and on its boundaries. Thanks to the greatly increased speed and memory storage of modern computers and also because of improved computational schemes as well as grid generation algorithms, now this problem is addressed mostly numerically. In this way it is possible to handle even complex geometries and obtain accurate solutions in a relatively short time. One of the most interesting problems that arise in heat transfer studies is when the solid body is immersed in an aerodynamic flow and

---

[*]PhD Student, Dipartimento di Ingegneria Aeronautica e Spaziale, Corso Duca degli Abruzzi 24, Torino, Italy, AIAA Member, (pietro.ferrero@polito.it).

[†]Assistant Professor, Dipartimento di Ingegneria Aeronautica e Spaziale, Corso Duca degli Abruzzi 24, 10129 Torino, Italy, AIAA Member, (domenic.dambrosio@polito.it).

its walls are thermally convective. This case, which is characterized by the interaction between heat transfer in the fluid and in the solid, is often called the Conjugate Heat Transfer Problem (CHT) in the literature. In the past, it was common to simplify the problem by calculating first the aerodynamic field and then evaluating the temperature inside the solid body separately, by imposing a prescribed heat wall flux or temperature at the interface. This could be acceptable for some applications, but it neglects the active coupling between the aerodynamic flow outside the body and the thermal field inside it. If realistic and accurate calculations of temperature fields are required, which are very important for evaluating thermal stresses and for the choice of a suitable material, then the full coupling has to be taken into account.

In this work, the coupling of a heat-conduction solver with an existing fluid dynamics solver will be investigated, with the objective of expanding the potentialities and domain of application of the latter.

Due to the importance and vast application of this problem in so many fields, papers over the last ten to fifteen years showed an increasing interest in the CHT problem.

Rahaim et al.[1] solved the heat equation inside the solid with a Boundary Element method, while a Finite Volume (FV) scheme is used for the Navier-Stokes equations: the advantage of this method is that the mesh inside the solid body is not required. A similar approach is carried out by He et al.[2] who apply a coupled Finite-Difference method / Boundary Element Method (FDM / BEM) to solve the incompressible flow inside a thick-wall parallel channel with constant wall temperature and constant heat flux boundary conditions. Webster[3] developed a heat transfer code, which he coupled with an existing fluid solver, in a similar manner as it is done in this work. Hassan et al.[4] presented an iterative loose coupling between a FV computational fluid dynamics code and a finite element material thermal response code and used it to study ablation phenomena on a reentry vehicle flying along a ballistic trajectory. Liu et al.[5,6] developed numerical schemes for tightly coupling fluid and solid solvers through the constant computation of the heat flux at the fluid/solid interface.

In summary, a lot of effort has been made to develop efficient and accurate techniques for coupling flow and solid heat conduction solvers. However, in many cases the coupling between the two was carried out using explicit boundary conditions, and that resulted in a loose coupling. There is still a lot of work to do to demonstrate that a strong coupling between the two solvers can be obtained for complex flows and geometries in practical problems. This paper tries to proceed in this direction by showing that the solid solver developed and then strongly coupled with the fluid solver is able to compute quite accurately temperature fields even for non trivial domains within an acceptable computational time. This is done by making some assumptions and neglecting some aspects of the problem, such as the possibility of thermal expansion, ablation or change of phase of the solid body. In addition, the simulated

material has to be isotrope, though not necessarily homogeneous.

The paper is organized as follows. First, the governing equations of both the fluid and the solid phases are presented. As one of the main goals of this work has been to develop and test a heat-conduction solver for solid bodies, more attention and emphasis will be given to describe the schemes and the algorithms used for this code rather than those used for the hypersonic flow solver. A subsequent part is devoted to show how the coupling of the two codes was achieved; such a coupling, which occurs only at the interfaces between the gas and the solid, represents the heart of the CHT problem. In the last section the results of some numerical experiments are presented. To start with, we run simple test cases using the heat solver only and we compare the results with an analytic solution, if available, or with the results of previous works. Subsequently, the fully coupled scheme is used to perform some numerical experiments on two different solid bodies: a hollow and a full bullet. Two different materials with thermally opposite characteristics are used, in order to enhance the differences in their thermal behaviors. In the final part, a validation case is presented: the wall temperature distributions on a blunt body is compared with those obtained experimentally in the wind tunnel facilities at DLR-Koeln, Germany. The comparison shows promising results and it emphasizes the strong influence exerted on the solution by the complete experimental setup.

II.   Governing equations

II.A.   Fluid Phase

The Navier-Stokes equations are used to model the behavior of the fluid:

$$\frac{d}{dt}\int_{\Omega_c} \mathbf{W}dV + \int_{\partial\Omega_c}(\mathbf{F}_v - \mathbf{F}_i)dA = \int_{\Omega_c}\dot{\mathbf{\Omega}}dV \tag{1}$$

This system of equations is discretized with a finite volume method, while an explicit scheme is adopted to march in time. Convective fluxes are evaluated using an upwind Flux-Difference Splitting (FDS) scheme.[7] Second order accuracy in space and time is obtained using ENO-like schemes.[8] The flow solver accounts for chemical and vibrational non-equilibrium phenomena. Viscosity, thermal conductivity and mass diffusion fluxes are obtained using Chapman-Enskog theory in the first nonvanishing approximation in terms of Sonine polynomials.

II.B. Solid Phase

The thermal behavior of the solid phase is modeled by the integral form of the heat equation, which is obtained by applying the principle of conservation of energy to a finite volume of matter:

$$\frac{d}{dt} \int_{\Omega_c} E dV + \int_{\partial\Omega_c} (\dot{\mathbf{q}} \cdot \mathbf{n}) dA = \int_{\Omega_c} R dV \tag{2}$$

There exists a relationship between temperature and solid state energy:

$$E = \int_{T_{ref}}^{T} \rho c(\tau) d\tau + E_{ref} \tag{3}$$

In order to compute the thermal fluxes the Fourier law is applied:

$$\dot{\mathbf{q}} = -k\nabla T \tag{4}$$

The general form of the heat equation is thus:

$$\frac{d}{dt} \int_{\Omega_c} \rho c(T) T dV + \int_{\partial\Omega_c} k(T) \nabla T \cdot \mathbf{n} dA = \int_{\Omega_c} R dV \tag{5}$$

The thermal conductivity k and the specific heat c are usually a function of temperature. For certain materials, however, their dependence on temperature is so small that it can be considered as constant: using this assumption, k and c can be taken out from the integrals, so that the equation reduces to:

$$\frac{d}{dt} \int_{\Omega_c} T dV + \int_{\partial\Omega_c} \nu_{th} (\nabla T \cdot \mathbf{n}) dA = \int_{\Omega_c} R dV \tag{6}$$

where $\nu_{th} = k/\rho c$ is the thermal diffusivity.

III.   Numerical methods

In this section an overview of the methods and algorithms used to build the solid-state heat solver and to couple it with the fluid solver is presented. To make the coupling between the two codes easier, the heat equation (2) is discretized using a finite volume technique also. Another reason for this choice is that this equation is valid for each finite volume in which the domain can be divided as well as for the whole domain itself: thus a FV scheme is inherently conservative. The volume integral of (2) is approximated by:

$$\int_{\Omega_c} E dV \approx E_c \int_{\Omega_c} dV = E_c \cdot V_c \tag{7}$$

here, the subscript c refers to the centroid of the cell. The heat source term, if present, is approximated in the same way.

The surface integral, which represents the heat fluxes, is modeled using a set of secondary cells staggered with respect to the primary ones.

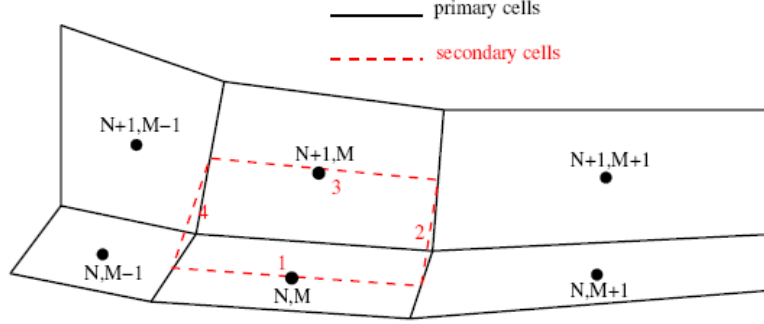Considering Figure 1 and applying the divergence theorem to the secondary cell:

Figure 1. Staggered cells

$$\int_{S_{sec}} T\mathbf{n}_x dS = \int_{V_{sec}} \frac{\partial T}{\partial x} dV \tag{8}$$

$$\int_{S_{sec}} T\mathbf{n}_y dS = \int_{V_{sec}} \frac{\partial T}{\partial y} dV \tag{9}$$

In this way it is possible to evaluate ∇T on the lateral surfaces of the primary cells. With reference to Fig. 1:

$$\left(\frac{\partial T}{\partial x}\right)_{N+1/2,M} = \frac{1}{\Delta V_{N,M}^{sec}} \left(T_1 n_{x_1}^{sec} S_1^{sec} + T_2 n_{x_2}^{sec} S_2^{sec} + T_3 n_{x_3}^{sec} S_3^{sec} + T_4 n_{x_4}^{sec} S_4^{sec}\right) \tag{10}$$

Similar relationships hold for the other surfaces of the primary cell.

The values of T on the secondary cells surfaces are given by:

$$T_1 = T_{N,M} \tag{11a}$$

$$T_3 = T_{N+1,M} \tag{11b}$$

$$T_2 = \frac{1}{2}\left(\frac{T_{N,M} S_{1_{N,M+1}}^{sec} + T_{N,M+1} S_{1_{N,M}}^{sec}}{S_{1_{N,M+1}}^{sec} + S_{1_{N,M}}^{sec}} + \frac{T_{N+1,M} S_{3_{N,M+1}}^{sec} + T_{N+1,M+1} S_{3_{N,M}}^{sec}}{S_{3_{N,M}}^{sec} + S_{3_{N,M+1}}^{sec}}\right) \tag{11c}$$

$$T_4 = \frac{1}{2}\left(\frac{T_{N,M} S_{1_{N,M-1}}^{sec} + T_{N,M-1} S_{1_{N,M}}^{sec}}{S_{1_{N,M+1}}^{sec} + S_{1_{N,M}}^{sec}} + \frac{T_{N+1,M} S_{3_{N,M-1}}^{sec} + T_{N+1,M-1} S_{3_{N,M}}^{sec}}{S_{3_{N,M}}^{sec} + S_{3_{N,M-1}}^{sec}}\right) \tag{11d}$$

where in the last two expression T_2 and T_4 are calculated by making an average of the neighboring values of T weighted with the secondary cells surfaces. The procedure is repeated for each face of the cell, in order to obtain the total flux entering or leaving the cell. This method is second order accurate in space; the stencil for the generic N, M cell is the shaded region sketched in Fig. 2; because of the symmetry of the heat equation, this choice for the stencil turns out to be quite adequate for the problem.

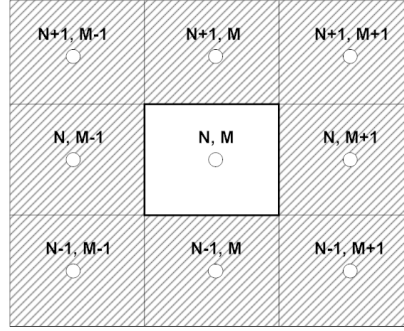At this point, neglecting the heat source term, an ordinary differential equation is obtained

Figure 2. Stencil of the numerical scheme

for each computational cell c:

$$\frac{dE_c}{dt}V_c = -\sum_{j=1}^{nf} k_j (\nabla T)_j \cdot A_j = \mathbf{F}_c\left[T_{stencil}, t\right] \tag{12}$$

where nf is the number of faces of a cell.

Since this equation must be valid for all the cells in the computational domain nc, Eq. 12 becomes a system of differential equations. Considering that the time scale of the heating/cooling process is much larger than that of fluid dynamics, an implicit integration scheme has been used, in order to avoid limitations on the maximum Δt that can be chosen. To integrate the system in time a first or second order scheme can be used. The former is an implicit backward Euler method and it reads:

$$\frac{\Delta E_c^{k+1}}{\Delta t}V_c = \mathbf{F}_c^{k+1}\left[T^{k+1}, t\right] \tag{13}$$

where $\Delta E_c^{k+1} = E_c^{k+1} - E_c^k$. The term relative to the fluxes at step $k+1$ can be approximated with a first order Taylor expansion:

$$\mathbf{F}_c^{k+1} = \mathbf{F}_c^k + \left(\frac{\partial \mathbf{F}_c}{\partial E}\right)^k \frac{\Delta E_c^{k+1}}{\Delta t}\Delta t \tag{14}$$

where the Jacobian of the problem is given by (omitting the subscript c):

$$\left(\frac{\partial \mathbf{F}}{\partial E}\right)^k = \left(\frac{\partial \mathbf{F}}{\partial T}\right)^k \left(\frac{\partial T}{\partial E}\right)^k = \left(\sum_{j=1}^{nf} k(T)_j \frac{\partial (\nabla T)_j}{\partial T} \cdot A_j + \sum_{j=1}^{nf} (\nabla T)_j \frac{\partial k_j(T)}{\partial T}\right)^k \left(\frac{\partial T}{\partial E}\right)^k$$

(15)

The second addenda is present only if the thermal conductivity is a function of temperature and must evaluated at each time step, while the term $\partial(\nabla T)_j/\partial T$ depends only on the geometry of the grid and can be calculated once and for all at the beginning of the computation. The derivative of the temperature with respect to the internal energy is given by:

$$\left(\frac{\partial T}{\partial E}\right)^k = \left(\frac{1}{\rho c + \rho c_T T + \rho_T c T}\right)^k$$

(16)

where c_T and ρ_T are the derivatives of c and ρ with respect to temperature: as their dependence on T is usually given as a polynomial, they have been evaluated analytically.

Finally, by substituting Eq. (15) into Eq. (13), we obtain the final algorithm that was employed in this study:

$$\left[\left(\frac{\partial \mathbf{F}_c}{\partial E}\right)^k - \frac{V_c}{\Delta t}\right] \Delta E_c^{k+1} = -\mathbf{F}_c^k[T^k]$$

(17)

The Jacobian matrix $\left(\frac{\partial \mathbf{F}}{\partial E}\right)^k$ is evaluated numerically by perturbing, one by one, every cell of the numerical domain and calculating the resultant perturbed flux.

If specific heat, c, and the density, ρ, are constant, the temperature is simply obtained as $T = E/\rho c$; otherwise, a Newton iterative method is employed.

To obtain second order accuracy in time, a Crank-Nicholson scheme can be used; in this case the fluxes are evaluated at the time step k+1/2 instead that at k+1, again using a Taylor expansion:

$$\mathbf{F}_c^{k+1/2} = \mathbf{F}_c^k + \left(\frac{\partial \mathbf{F}_c}{\partial E}\right)^k \frac{\Delta E_c^{k+1}}{\Delta t} \frac{\Delta t}{2}$$

(18)

so that the resultant scheme is:

$$\left[\frac{1}{2}\left(\frac{\partial \mathbf{F}_c}{\partial E}\right)^k - \frac{V_c}{\Delta t}\right] \Delta E_c^{k+1} = -\mathbf{F}_c^k$$

(19)

The Crank-Nicholson scheme, compared to the backward Euler, is only marginally stable and so it must be used with more caution in presence on very stretched meshes or Neumann boundary conditions.

The linear system 17 (or 19) is solved using a GMRES iterative method; the matrix is

preconditioned with an incomplete LU factorization. The routines for preconditioning and solving the system have been developed by Saad.[9]

III.A.   Coupling fluid and solid models

The coupling of the two codes is a process of extreme importance. If the goal is to obtain time-accurate results, a tight coupling between the two must be enforced. The fluid and solid codes are coupled together by solving a balance equation of heat fluxes at the interface between the two phases:

$$\dot{q}_{tot} = \dot{q}_{cond} + \dot{q}_{diff} + \dot{q}_{vib} + \dot{q}_{rad} + \dot{q}_{sol} = \dot{q}_{fluid} + \dot{q}_{sol} = 0 \tag{20}$$

where $\dot{q}_{cond} = -k_{fluid}\vec{\nabla}T \cdot \vec{n}$ is the convection heat flux inside the fluid; $\dot{q}_{diff} = \sum_{i=1}^{NSPE} J_{m_i}h_i$ is the heat flux due to the mass diffusion in the fluid for every chemical species i with enthalpy h_i; $\dot{q}_{vib} = -k_{vib}\vec{\nabla}T_{vib} \cdot \vec{n}$ is the heat flux due to vibrational energies, modeled using the vibrational temperatures T_{vib}; $\dot{q}_{rad} = \epsilon\sigma T_W^4$ is the radiative heat flux, while the thermal flux inside the solid body is $\dot{q}_{sol} = -k_{sol}\vec{\nabla}T \cdot \vec{n}$.

The balance equation (20), thus, is a non linear equation with temperature as unknown in the form $F(T_W) = 0$ and it is numerically solved using an iterative Newton method. Each new iteration step is given by:

$$T_W^{i+1} = -\frac{F(T_W^i)}{\partial F/\partial T_W} + T_W^i \tag{21}$$

The derivative $\partial F/\partial T$ is computed numerically by perturbing of a small δT and evaluating the perturbed function:

$$\frac{\partial F}{\partial T_W} \approx \frac{F(T_W^*) - F(T_W)}{\delta T} \tag{22}$$

The cycle continues until $|T_W^{i+1} - T_W^i|$ drops below a certain tolerance; convergence is usually achieved in very few steps.

A tight coupling between the two codes is established because the wall heat fluxes in the solid and in the flow mutually contribute to define the wall temperature, which in turn affects both the temperature field in the body and the flow field. By solving Eq.(20), T_W is computed for every cell surface lying on the fluid/solid interface and it is used as a fixed temperature boundary condition for both the flow and the solid-body heat conduction solver. At each integration step, the heat equation is solved using a time-step $\Delta t_{sol} = \Delta t_{fluid}$ and a new temperature field is determined. The same is done with the flow solver. The new temperature fields in the solid body and in the flow modify the value of $\dot{q}_{sol}$ and $\dot{q}_{fluid}$ and, therefore, the wall temperature also. This process is repeated, for all the cells that compose the solid-fluid

interface, for every time step during the integration, so that both the aerodynamics and the temperature field inside the body evolve simultaneously.

For unsteady problems, where time-accurate solutions are sought for, the same Δt is used for marching in time both the fluid and the solid phase solutions. However, if an explicit method for the fluid is used, the maximum Δt_{fluid} can be very small and the computational time required can be very high. Therefore, for steady problems, it is possible to use two different Δt for the fluid and the solid, but, in this case, the simultaneous evolution of the two fields is lost. A hybrid coupling strategy can still be enforced by considering the time evolution as composed of a series of *quasi-stationary* states. In this case, the solid solver is free to advance in time (without limitations on the maximum Δt) until the wall temperature in one of the cells at the interface grows too much (to this purpose, a threshold value for the maximum admissible ΔT_W can be prescribed). When this happens, the two codes are run together again, at the same Δt, until all the residuals of fluid dynamics drop below a certain value (which usually depends on the considered problem). Using this technique the heat flow inside the body is simulated much more faster, while the flow field is allowed to "relax" and to adjust to the small changes in the wall temperature.

IV.   Numerical Results

IV.A.   Heat Conduction Solver Test Cases

Before coupling the heat conduction solver with the fluid solver, we must demonstrate that the former works properly and that it is able to obtain accurate and consistent results. For this reason, two simple test cases were run and the obtained results are compared with an analytical solution or with those obtained in previous works.

IV.A.1.   Test ♯ 1: Comparison with an analytic solution

As the only purpose of a validation test is to examine the capacity of a scheme to solve the differential equation, a real physical solution is not necessarily required. So, in this first experiment, we follow the approach proposed by Roache[10] and we choose an analytical function as the solution of the differential equation.

The chosen function is:
$$T(x, y, t) = A(2 - e^{-\nu_{th} t}) \sin x \sin y \tag{23}$$

which is the analytical solution of:
$$\rho c \frac{dT}{dt} + \nabla \cdot (-k \nabla T) = g(x, y, t) \tag{24}$$

where:

$$g(x, y, t) = A(4 - e^{-\nu_{th}t}) \sin x \sin y \tag{25}$$

For simplicity, all the thermal coefficients (ρ, c, k and ν_{th}) are set to be one. The computational domain is the square $[0, \pi] \times [0, \pi]$, and $A = 5$. Boundary and initial conditions can be easily evaluated. The analytical and the numerical solutions after $t = 1$ s are compared using infinite and second norm:

$$E_\infty = max \, \|T_N(x, y, t) - T_A(x, y, t)\| \tag{26}$$

$$E_2 = \sqrt{\sum^{NC} [T_N(x, y, t) - T_A(x, y, t)]^2 dv} \tag{27}$$

where T_N is the numerical solution, T_A the analytic one, NC is the total number of cells and dv is the volume of each cell.

In order to investigate the spacial convergence of the scheme, equally spaced grids with 10, 20, 40, 80 and 160 cells per sides are used. The time step used for each case is decreased accordingly, by imposing that the Fourier number ($Fo = \frac{\nu_{th}\Delta t}{\Delta x^2}$) remains at the constant value of 1. The log plot of Fig. 3 shows that the present scheme is second order accurate in space both in the second and in the infinite norm.

To verify the time convergence of the scheme the grid is held constant, while the time steps
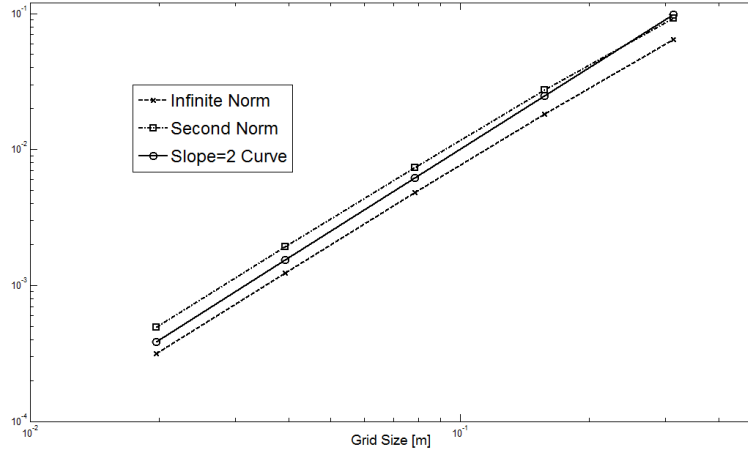
Figure 3. Norm 2 and Infinite Norm for space convergence

are progressively decreased. The grid size selected is small enough so that space errors can be considered negligible compared to temporal ones. The grid is made up of 640×640 cells equally spaced and the computation is carried on using time steps of 0.2, 0.1, 0.05, 0.025, 0.0125 and 0.00625 seconds. A log plot of the second and infinite norm is shown in Fig. 4 for both the first (Eq. 17) and second order scheme (Eq. 19); considering the slopes of

the curves, it is demonstrated that the two schemes are respectively first and second order accurate in time. The slight deviation from second order that the error norm plots display for very small Δt is due to round off errors.
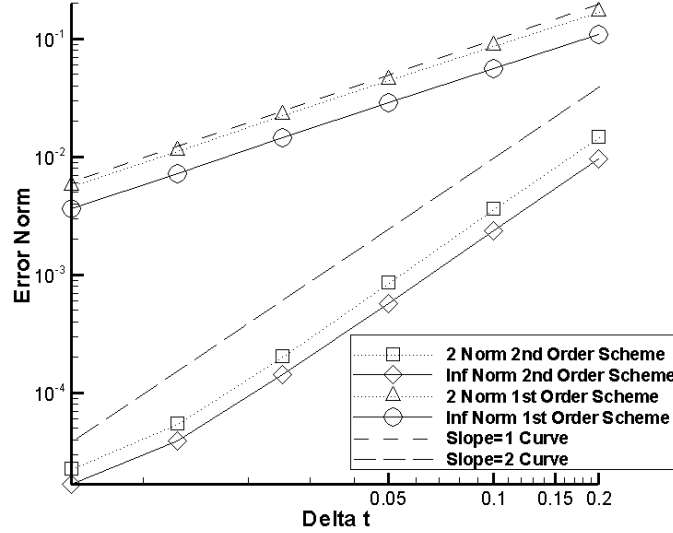

Figure 4. Norm 2 and Infinite Norm for time convergence

IV.A.2. Test ♮ 2: Bidimensional Composite Solid

In this second experiment, the capability of the solver to handle multi-block domains made with different materials is tested. Here, an analytical solution is not available and the comparison will be done with the numerical results by Liu.[6]

The setup and the boundary conditions are the same proposed by Liu. A rectangular domain $0.3 \times 0.9\ m$ is equally divided into three sub blocks. Each sub-block is made of a different material and it is discretized using 51×51 points. A constant heat flux of $9000\ W/m^2$ is imposed on the lower surface, while the other three boundaries are held at a fixed temperature of $400\ K$. The initial temperature is $300\ K$ and the simulation lasts for 80 seconds with a $\Delta t = 0.01\ s$. The materials used in the simulations together with their thermal characteris-

	$\mathbf{k}\ [W/(mK)]$	$\rho\ [Kg/m^3]$	$\mathbf{C}\ [J/(KgK)]$	$\nu_{th}\ [m^2/s]$	$T_{melt}\ [K]$
Copper	401	8920	384.91	$1.1676 \cdot 10^{-4}$	1350
Aluminium	204	2720	895	$8.38 \cdot 10^{-5}$	933
Bronze	26	8670	340	$8.82 \cdot 10^{-6}$	727
Brass	104	8520	380	$3.21 \cdot 10^{-5}$	735

Table 1. Thermal properties at 300 K of the materials used in the simulations of test ♮ 2

tics, taken from Incropera,[11] are listed in Table 1.

In Figure 5, 6 and 7, the temperature fields obtained using pure copper, copper/aluminium
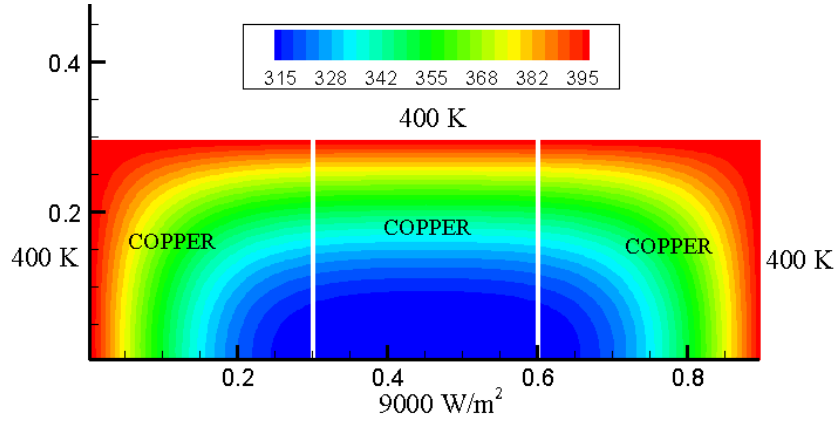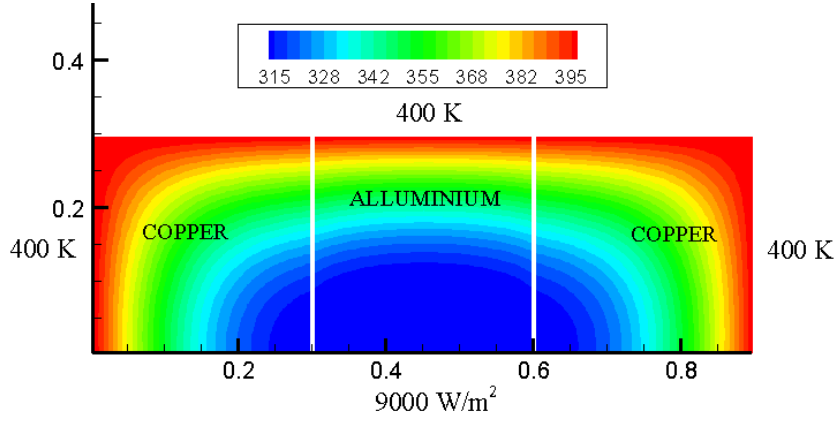
Figure 5. Temperature for three copper blocks at $t = 80\ s$

Figure 6. Temperature field for copper-aluminium blocks at $t = 80\ s$
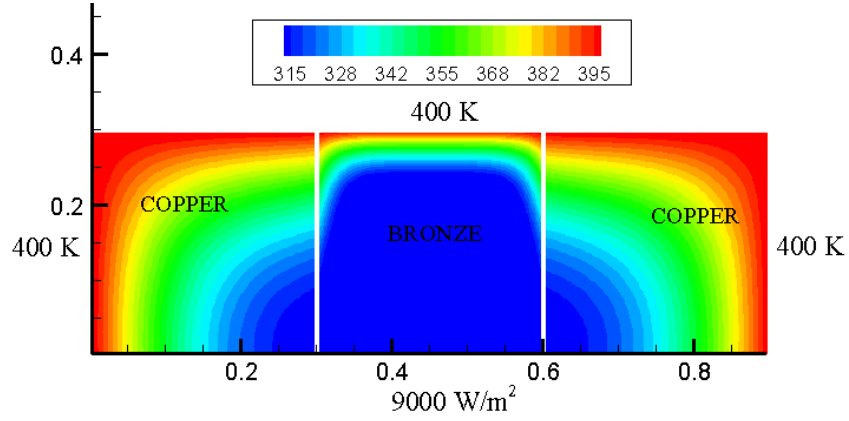

Figure 7. Temperature for copper-bronze blocks at $t = 80\ s$

and copper/bronze respectively are shown. These results are in good agreement with those obtained by Liu. In addition, the solid heat transfer solver converged fast and well even in

domains made up of different materials.

A more interesting result is obtained when three different materials, copper, brass and
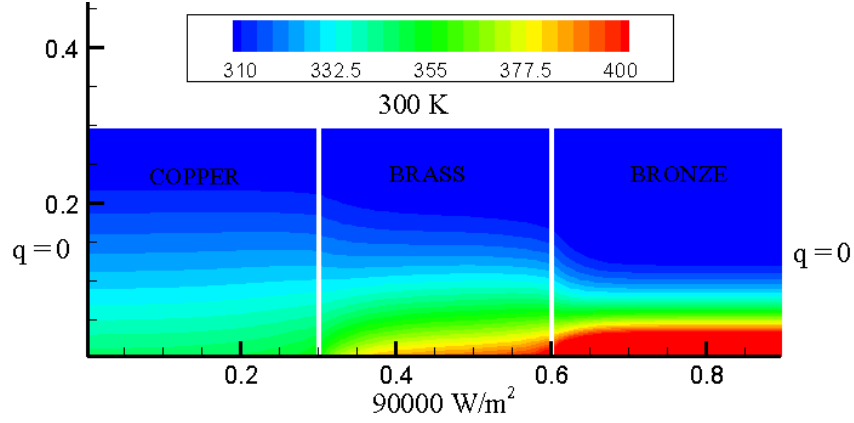
Figure 8. **Temperature for copper-brass-bronze blocks after** $300\ s$

bronze, are used together. In this case a heat flux of 90000 W/m^2 is imposed at the bottom boundary, the left and right surfaces are adiabatic, while the top one is held at 300 K. The initial temperature and the time step are the same of the previous experiments. It can be seen (Fig. 8) that heat transfers faster in copper than in brass and bronze, according to their respective thermal diffusivity. Furthermore, more heat is transferred from copper to brass than from brass to bronze.

IV.B.   Coupled Heat Conduction and Fluid Solvers

In this section, the results obtained by coupling the solid heat solver with the flow solver are presented. The first four experiments deal with a homogeneous hemisphere/cylinder configuration which has been simulated using two different materials and two different geometrical setups.

The other case presented is for validation: the heating of a double cone body made of an UHTC material is compared with some available experimental results.

IV.B.1.   Homogeneous hemisphere/cylinder configuration in a flow at Mach 17

For these experiments two different geometric configurations are selected: a hollow body and a full body.

Building a grid to discretize the latter was a challenging task because of the topology of the domain: the fluid and the solid solvers are able to manage only quadrilateral cells, which are hard to fit inside a convex domain without distorting them too much. To overcome this problem a grid mapping was used to convert a quadrilateral domain into a circular one;[12] the grid obtained with this technique is shown in Fig. 10.

The freestream conditions of the hypersonic flow are listed in Table 2 and are the same for
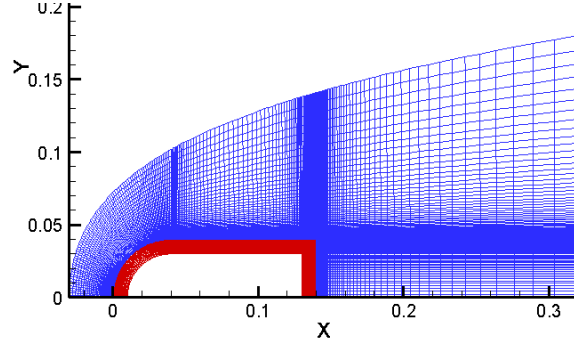

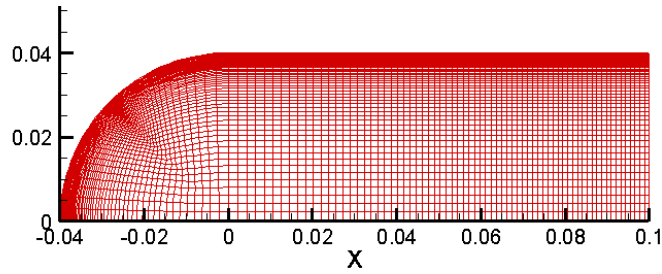**Figure 9.** Hollow bullet grid together with the fluid one

Figure 10. Grid used for the full bullet

M_∞	17.0
p_∞ [Pa]	10.0
T_∞ [K]	200.0
Fluid Type	Air with 5 species considered

Table 2. Characteristic of the flow

all tests. The boundary conditions employed are a supersonic inlet and outlet, a symmetry condition at the center line and a no-slip, fully-catalytic thermally-convective wall is enforced at the solid/fluid interface. In the case of the hollow bullet, an adiabatic condition is imposed on the internal boundary.

For these simulations two different kind of materials have been used: a very good heat conductor, copper, and a glass ceramic called MACOR. The thermal properties of MACOR are listed in Table 3. Both materials have comparable thermal capacity (the product of ρ and c), but the coefficient of thermal conductivity differs of many orders of magnitude. This choice was made in order to emphasize as much as possible the different responses of the two materials in the same aerodynamic environment.

In order to obtain results with a reasonable computational effort, the solid and the fluid solvers are run at the same Δt only until the aerodynamic field becomes steady around

	k $[W/(mK)]$	ρ $[Kg/m^3]$	**C** $[J/(KgK)]$	ν_{th} $[m^2/s]$	T_{melt} $[K]$
Copper	401	8920	384.91	$1.1676 \cdot 10^{-4}$	1350
MACOR	1.46	2520	790	$7.334 \cdot 10^{-7}$	1273

Table 3. Thermal properties at 300 K of MACOR and copper

the body, with the only exception represented by the wake. When this happens, the Δt which is used to integrate the heat equation is largely increased and the two fields evolve through a series of *quasi-stationary* states, as described more in detail in Sec. III.A. In all the calculations a second order accurate method both in space and time was employed, with a $\Delta t_{sol} = 5 \cdot 10^{-3} s$.

In Figure 11 we show temperature and Mach number in the flow field at steady state (at $t = 0.6 \ ms$); the temperature inside the body had not enough time to change significantly. A very similar flow field is found in the case of the full body, because the external shape and size of the body are the same.

The temperature field obtained after 90 s is shown in Fig. 12.
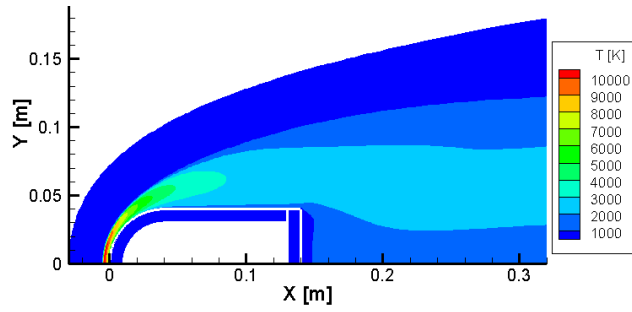
Figure 11. Temperature field outside and inside the body after $t = 0.6 \ ms$
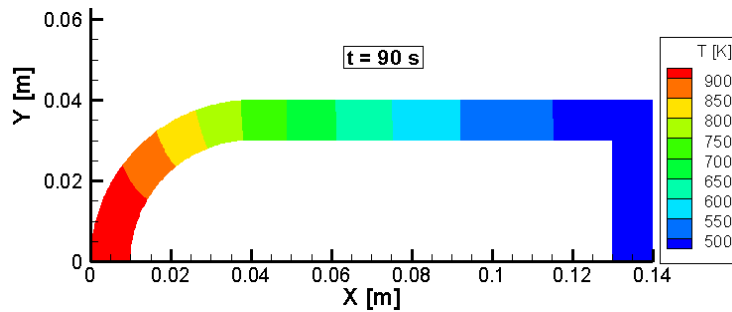

Figure 12. Temperature field after 90 s

In the case of the full body, the main difference with respect to the hollow one is that the temperatures reached are lower. This is due to the fact that the full body is more massive

than the hollow one so that the thermal load is more spread and the temperatures remain lower.

As the thermal conductivity and the specific heat of metals are dependent on temperature
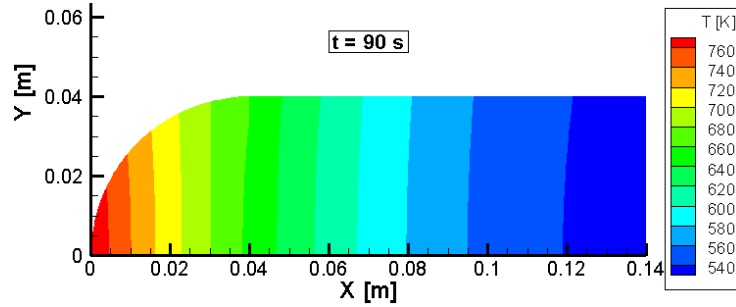

Figure 13. Temperature field after 90 s for copper

and, thus, on location, another simulation with a 4th order polynomial interpolation of experimental data[11] was adopted for both k and c:

$$k = a_0 + a_1 T + a_2 T^2 + a_3 T^3 + a_4 T^4 \tag{28}$$

$$c = b_0 + b_1 T + b_2 T^2 + b_3 T^3 + b_4 T^4 \tag{29}$$

The evolution of temperature at the stagnation point after 90 s is shown in Fig. 14 for the two cases. The main observation is that neglecting the dependence of k and c from temper-
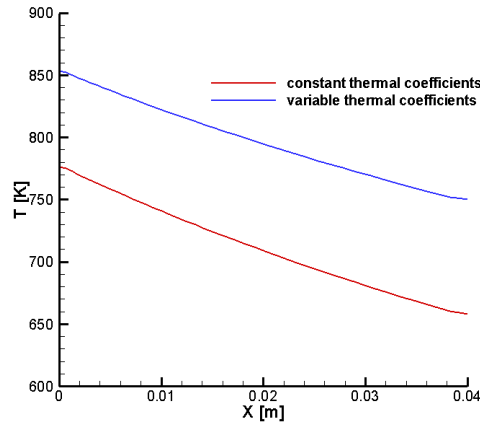
Figure 14. Temperature field after 90 s on the nose of the full bullet considering constant and variable thermal coefficients

ature may cause pretty large errors, especially if high temperatures are reached, as in this experiment. In the case of copper, using fixed thermal coefficients causes an underestimation of the thermal heating of the body.

The pattern of the temperature field is very different if we change the material of the body from a metal to an insulator, while keeping fixed all the other aerothermodynamic parame-

ters. In these latter cases almost all of the heating is confined in a thin layer very close to the interface, the so called "skin", where temperature can be very high: after few seconds it exceeds the melting point of the material, which is $1273\ K$. On the contrary, on the metallic body, the heating is spread more efficiently through the body, so that the maximum temperature reached after the same time interval is much lower.

The results for the hollow and solid bullets after $30\ s$ are reported in Fig. 15 and 16
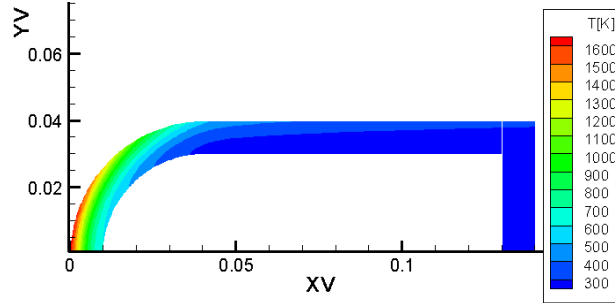
Figure 15. Temperatures inside a hollow MACOR body after $30\ s$
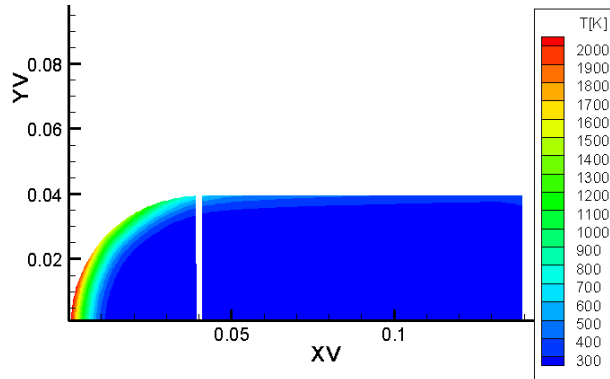
Figure 16. Temperatures inside a full MACOR body after $30\ s$

respectively. The differences within the two domains are very limited, because, as already pointed out, the heating is concentrated on the outer layers and "protects" the bulk of the body: however it is interesting to notice that the temperature reached close to the interface are higher for the full case body.

IV.C.   Validation Case

This simulation tries to replicate an experiment performed in the L2K wind tunnel at DLR Koeln in Germany[a]. The body is an axi-symmetric double cone made of a class of materials

called UHTC (Ultra High Temperature Material), whose average thermal characteristics are shown in Tab. 4. On the back of the body an adiabatic condition is imposed and the initial temperature is 300 K. A drawing and a CAD model of the specimen used in the experiment are shown in Fig. 17.

The main characteristics of the flow and of the body walls are listed in Tab. 5 and Tab. 6.
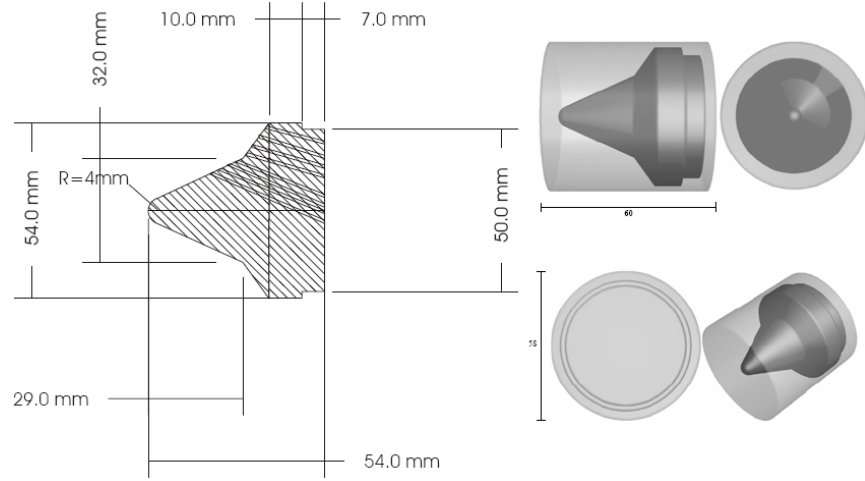
Figure 17. Drawing of the body (left) and CAD model (right)

	$\mathbf{k}$ $[W/(mK)]$	ρ $[Kg/m^3]$	$\mathbf{C}$ $[J/(KgK)]$	ν_{th} $[m^2/s]$
UHTC	66	6000	628	$1.7516 \cdot 10^{-5}$

Table 4. Average thermal properties of UHTC class materials

M_∞	4.57	y_N	0.000
p_∞ [Pa]	272.0	y_{NO}	0.000
T_∞ [K]	764.0	y_{O_2}	0.113
y_O	0.092	y_{N_2}	0.739

Table 5. In flow conditions for the DLR experiment

The temperature field around the body at the beginning of the simulation (i.e. when the body is still at the initial temperature of 300 K) is shown on Fig. 18. The typical structure of a shock wave - boundary layer type V interaction is present in the front part of the body, with a separation shock, a reattachment shock and a separated flow region, whose size strongly depends on the wall temperature. The thermography data available refers to the time history of the wall temperature at 4 mm and at 35 mm from the body nose, for a total simulation time of 90 s; $x = 0$ is on the leading edge of the blunted cone. The numerical simulations have been carried out using the quasi-stationary approach: different thresholds

Material type	UHTC
Catalytic behavior	Fully Catalytic
Emissivity factor	0.85

Table 6. Wall characterization
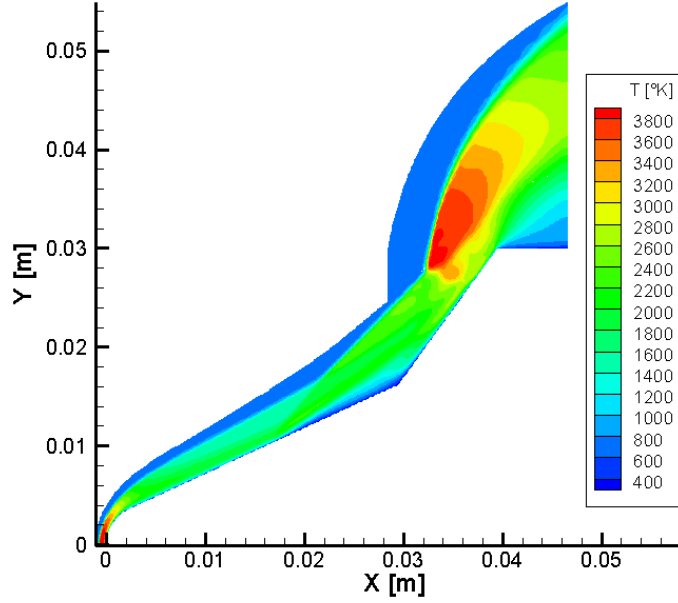
Figure 18. Temperature field around the body at the beginning of the simulation

between the solid and the fluid solvers have been used in order to check their influence. The method employed to integrate in time was second-order accurate with a $\Delta t = 1 \cdot 10^{-3}$ s. The comparison between the numerical results with two different thresholds and the experimental measurements at $x = 4$ mm from the nose of the body is shown in Fig. 19. The writing "threshold 0.5% (or 5%)" indicates that the heat equation solver was run in a loosely coupled fashion until the local wall temperature increase at any point of the fluid/solid interface was lower than 0.5% (or 5%). Then the two codes are again run together in a tightly coupled fashion until fluid dynamics had relaxed again (see Par. III.A).

All the calculations, and especially those with lower thresholds, which are more accurate, predict higher temperatures than those measured experimentally. This discrepancy most probably lies in the fact that, on the back wall of the body, an adiabatic condition is imposed, i.e. no heat flux is leaving the body. In reality, during the experiment, the double cone is held in its position by a copper prop, which, in turn, is attached to a structure that holds the specimen inside the hypersonic wind tunnel. In order to take into account at least the effect of the prop, both the fluid and solid grids were stretched out (Fig 20): the backward part of the latter was considered to be made of copper, like the prop, and on the back wall an adiabatic condition was imposed.
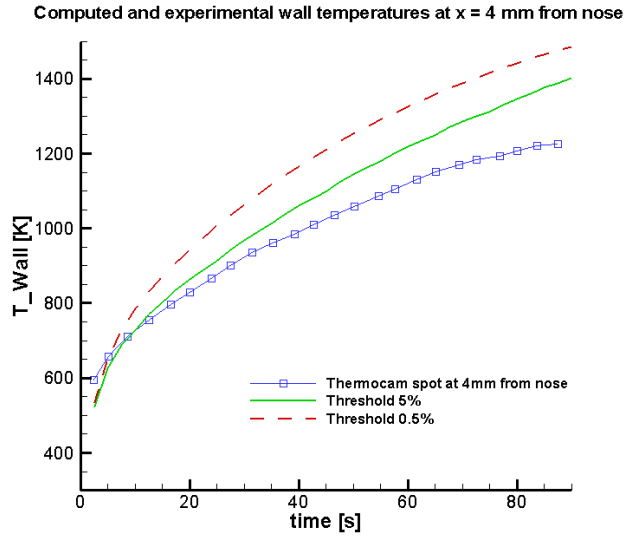
Figure 19. Time histories of Wall temperatures at $x = 4\ mm$ with two different thresholds and comparison with experimental values

The wall temperatures with this new configuration at two different locations on the double
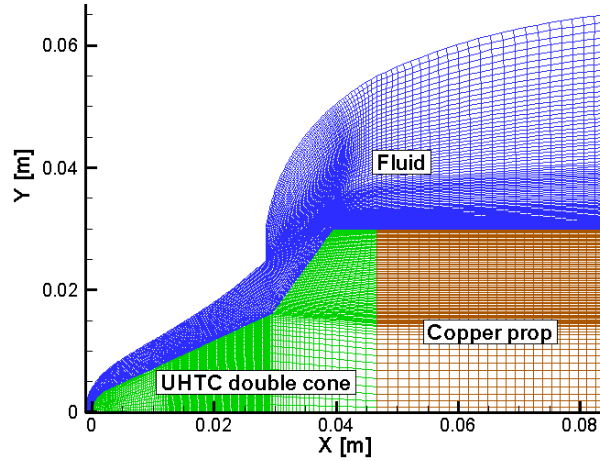

Figure 20. Grid used to simulate the double cone and its support

cone are shown in Fig. 21. No experimental data is available below $500\ K$ because this is the lower limit of sensitivity of the thermo-camera.

In Fig. 22 the distribution of the wall temperatures along the body after $60\ s$ is reported. The computed values lie very close to the experimental ones, except that at the hinge point between the two cones. The reason for this discrepancy is not clear at this time.

The results with the lengthen configuration show a good agreement with the experimental ones, and are much more accurate than those obtained before stretching the body. This implies the fact that, in CHT problems, neglecting the bottom parts of the solid body, even if they are far from the hottest part of the gas, can heavily affect the results of the front part
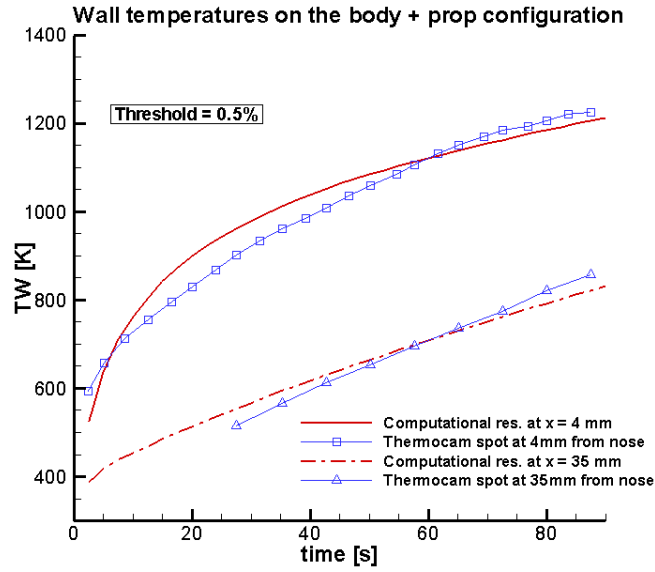
Figure 21. Time histories of wall temperatures at $x = 4\ mm$ and at $x = 35\ mm$ obtained with the stretched domain and comparison with the experimental values

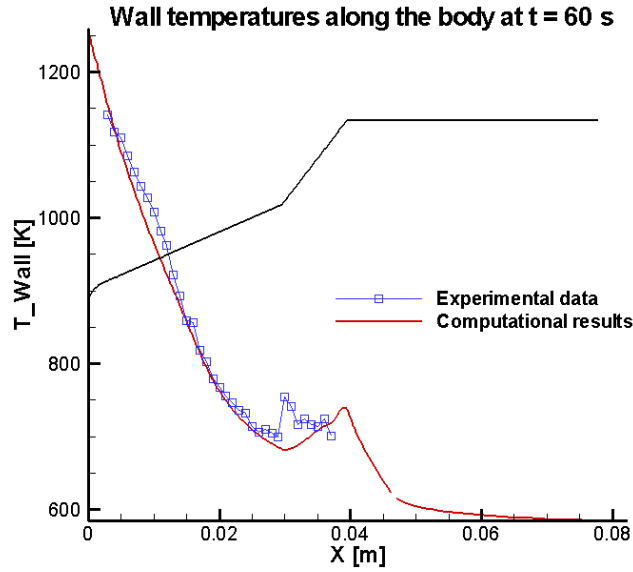**Figure 22.** Computed and measured wall temperatures along the body at $60\ s$

also.

Finally, the total heat fluxes entering the body and the internal temperature field are shown at the end of the simulation ($t = 90\ s$) in Figs. 23 and 24. Apart from the leading edge, the heat fluxes have a peak also at the at the base of the second cone, close to the bubble. This peak corresponds to higher temperatures inside the body in that region.

In all these calculations, the computer time for solving an iteration of the Poisson module has always been approximately 1% of the time employed for an iteration by the fluid dynamic
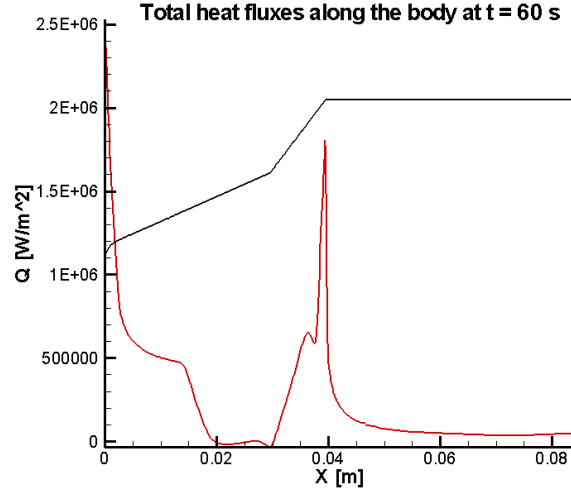
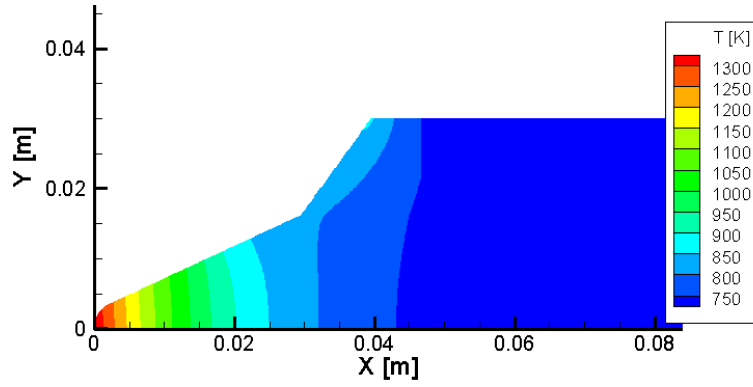**Figure 23.** Total heat fluxes entering the body at $t = 90 \ s$

Figure 24. Temperature field inside the double cone at $t = 90 \ s$

solver.

V.   Conclusions

In this paper we described how a solid-state heat solver was developed and coupled with a high-temperature hypersonic solver in order to improve and expand the range of application of the latter. The two codes were tightly coupled by imposing and solving iteratively a heat flux balance equation at the solid/fluid interface. The heat solver alone has proved to be reliable, accurate and fast by comparing some numerical results with analytical solutions or with previous works. When coupled to an explicit fluid solver, which has strict Δt_{max} limitations, a larger Δt for the solid solver was employed and the coupling was obtained through a series of quasi-stationary states.

The coupling has been tested on several domains made up of different materials. The compar-

ison with experimental data show overall a fair good agreement, provided that a sufficiently low threshold technique is chosen and that the geometry of the problem is well known and simulated.

As this scheme is able to handle domains made of different materials and with variable thermal coefficients, it could be easily employed on more practical engineering problems: the heating of the nozzle of a hypersonic wind tunnel or a preliminary estimation of the heating rate of an object flying at high Mach numbers are just two examples of the wide range of applications.

Further improvements may be done to remove some of the simplifications made and to expand the capabilities of the scheme. One interesting development would be to include the possibility of simulating an ablating material. Also, the same code may be extended to take into account changes in the body geometry due to ablation or to thermal expansion.

References

[1]Rahaim, P., "A Coupled DRBEM/FVM Approach to Transient Conjugate Heat Transfer," *Journal of Thermophysics and Heat Transfer*, Vol. 14, No. 1, 2000 pp. 27–38.

[2]He, M. et al., "A Coupled FDM/BEM Solution For The Conjugate Heat Transfer Problem," *Numerical Heat Transfer, Part B: Fundamentals*, Vol. 28 No. 2, 1995 pp. 139–154.

[3]Webster, R. S., "A Numerical Study of the Conjugate Conduction-Convection Heat Transfer Problem," *Ph.D. Dissertation*, Dept. of Aerospace Engineering, Mississippi State Univ., Mississippi State, MS, May 2001.

[4]Hassan, B., Kuntz, D., Potter, D. L., "Coupled fluid/thermal prediction of ablating hypersonic vehicles," *AIAA Paper 98-0168*, 1998.

[5]Liu, Q. W., Luke, E. A., Cinnella, P., "Coupling Heat Transfer and Fluid Flow Solvers for Multidisciplinary Simulations," *Journal of Thermophysics and Heat Transfer*, Vol. 19, No. 4, 2005 pp. 419–427.

[6]Liu, Q. W., "Coupling Heat Transfer and Fluid Flow Solvers for Multi-Disciplinary Simulations," *Ph.D. Dissertation*, Dept. of Aerospace Engineering, Mississippi State Univ., Mississippi State, MS, Aug. 2003.

[7]M. Pandolfi, "A Contribution to the Numerical Prediction of Unsteady Flows," *AIAA Journal*, Vol. 22, No. 5, 1983 pp. 602–610.

[8]A. Harten and B. Engquist and S. Osher and S. R. Chakravarthy, "Uniformly High Order Accurate Essentially Non-Oscillatory Schemes, III," *Journal of Computational Physics*, Vol. 71, Part 5, 1987 pp. 231–303.

[9]Yousef Saad, "'Iterative Methods for Sparse Linear Systems", *SIAM, Society for Industrial and Applied Mathematics*, 2000.

[10]Roache, P. J., "'Verification and Validation in Computational Science and Engineering.", *Albuquerque, NM: Hermosapublishers*, 1998.

[11]Incropera, F. P., DeWitt, D. P., "'Fundamentals of Heat Transfer," *John Wiley and Sons*, Appendix A, 2002.

[12]Donna, A. Calhoun, et al., "Logically Rectangular Grids and Finite Volume Methods for PDEs in Circular and Spherical Domains," 2006, http://www.amath.washington.edu/~rjl/pubs/circles/circles_revised.pdf

[13]Tran, H. K., Johnson, C. E., Rasky, D. J., et al., "Phenolic Impregnated Carbon Ablators (PICA) as Thermal Protection Systems for Discovery Missions," *NASA TM 110440*, April 1997.